MNRAS 000, 1–15 (2023) Preprint 30 August 2024 Compiled using MNRAS LATEX style file v3.2

A Monte Carlo Simulation Analysing the Likelihood of SLR Enrichment via Sequential Star Formation

Lewis Woods

30 August 2024

ABSTRACT

Numerous theories have been put forward to explain the above-galactic-background concentrations of ^{26}Al and ^{60}Fe in the Early Solar System (ESS). These short-lived radionuclides (SLRs) strongly influence planet habitability and were the dominant source of radiogenic heating in the early Earth. Enrichment via sequential star formation (SSF) is one theory shown to be capable of reproducing the SLR content of the ESS. Despite this, no statistical analyses of its feasibility are currently available – as there are for theories of direct enrichment from Core-Collapse Supernovae or AGB stars. A Monte Carlo simulation has been carried out to determine the viability of SSF as a source of ^{60}Fe enrichment. Two models of the dilution of supernova ejecta were used to provide results between two extremes. The probability of producing planetary systems matching the solar ^{60}Fe content was low (∼0.05% under the most generous dilution model). This is significantly lower than the probabilities of ∼1% found for direct enrichment mechanisms. Adjustments to the constraints of this theory may close this gap, yet SSF would remain no more viable than direct enrichment. Future work should incorporate an analysis of the ^{26}Al content yielded by this mechanism, and use hydrodynamical simulations to understand this process in greater detail.

1 INTRODUCTION

Short-lived radionuclides (SLRs) are radioactive isotopes which decay within 100Myr. Two SLRs, ^{26}Al and ^{60}Fe (with mean lifetimes of 1.1Myr and 3.7Myr respectively), dominated the radiogenic heating of the young Earth (McDonough et al. 2020).

SLRs impact a planet's geophysical evolution and habitability. Determining their origin in the Early Solar System (ESS) will shed light on the Sun's natal environment. As such, they have been of interest across many fields for several decades (Wasserburg 1985; Podosek & Nichols 1997; Adams 2010; Pfalzner et al. 2015; Lugaro et al. 2018; Busso 2018).

The radiogenic heating from ^{26}Al holds much sway over a planet's water content. A high ^{26}Al content drives the evaporation of water, producing dry worlds, while a relative lack of heating from low levels of ^{26}Al is likely to produce ice-covered worlds (Lichtenberg et al. 2019).

It has also been suggested that the development of technological civilisations is heavily influenced by a planet's ^{26}Al content (Gilmour & Middleton 2009). As a result, an understanding of the different mechanisms of such chemical enrichment (and their feasibility) will have significant implications for the field of astrobiology and the search for extraterrestrial life.

Since star and planet formation occur contemporaneously (Alves et al. 2020), the environment of the Sun's birth can be inferred from the circumstances that produced SLR enrichment in the ESS. Thus, determining the mechanism by which the ESS acquired its SLR abundance has become key to uncovering the Solar System's genealogy.

1.1 SLRs in the ESS

The galactic background abundance of SLRs can be determined through observation of the interstellar medium (ISM). For example, the concentrations of ^{26}Al and ^{60}Fe in the galactic background can be measured using observations of γ-ray emission lines (Diehl et al. 2006; Wang et al. 2007).

For now-decayed SLRs in the ESS, their prior presence must be inferred through a present-day excess of their decay products. For example, ^{26}Al will decay to extinction within ∼1.1Myr, leaving behind the daughter isotope ^{26}Mg. When studying solid materials in the Solar System, the excess of ^{26}Mg over the more stable ^{24}Mg provides the initial concentration of ^{26}Al. Similarly, the concentration of ^{60}Fe in the ESS is often reported as the mass ratio between itself and the more stable isotope ^{56}Fe.

In comparing galactic background measurements with meteoritic analysis of the oldest solids in the Solar System, it was determined that the ESS hosted greater abundances of 5 SLRs – ^{10}Be, ^{26}Al, ^{36}Cl, ^{41}Ca, and ^{60}Fe. Being 4567-4568Myr old, these solids indicate that the solar system acquired this chemical enrichment during, or immediately after, its formation (Tissot et al. 2017).

The presence of ^{10}Be, ^{36}Cl and ^{41}Ca can be explained by Cosmic Ray Spallation (CRS) – the process by which cosmic rays break apart heavy nuclei in the protoplanetary disc, creating an inhomogeneous distribution of lighter isotopes (Gounelle et al. 2006; Duprat & Tatischeff 2007; Jacobsen et al. 2011). However, CRS cannot produce ^{60}Fe and cannot account for the homogeneous distribution of ^{26}Al in the ESS. Thus, despite being the dominant sources of radiogenic heating in the ESS (McDonough et al. 2020), the origin of these two key SLRs remains contested.

Aside from CRS, there are three known mechanisms for ^{26}Al production, two of which also produce ^{60}Fe (see Table 1). Consequently, there are four main theories put forward as the origin of these last two unexplained SLRs: direct enrichment from Wolf-Rayet winds, Core-Collapse Supernovae (CCSNe), or AGB stars, and enrichment via sequential star formation (SSF). Each of these will be discussed in turn, with a brief consideration of their respective strengths and weaknesses as sources of SLR enrichment in the ESS.

© 2023 The Authors

Mechanism	^{26}Al Production	^{60}Fe Production	Reference(s)
Cosmic Ray Spallation	Yes	No	Gounelle et al. (2006)
WR Star Winds	Yes	No	Arnould et al. (1997, 2006)
AGB Star Winds	Yes	Yes	Lugaro et al. (2012)
Core-Collapse Supernova Ejecta	Yes	Yes	Limongi & Chieffi (2006, 2018); Thielemann et al. (2018)

Table 1. This table presents a summary of the four mechanisms known to produce ^{26}Al. Cosmic Ray Spallation and Wolf-Rayet winds produce ^{26}Al, whereas AGB stars and Core-Collapse Supernovae produce both ^{26}Al and ^{60}Fe.

1.2 Direct Enrichment from Wolf-Rayet Winds

The Wolf-Rayet (WR) phase of stellar evolution is characterised by strong winds which eject vast amounts of material. Progenitors of WR stars are initially at least 25M$_\odot$ in mass (Crowther 2007).
It has been shown that WR winds can account for the abundance of ^{26}Al in the ESS (Arnould et al. 1997, 2006). Despite this, WR stars do not produce ^{60}Fe, meaning they alone cannot explain the SLR enrichment of the ESS. Therefore, some source of ^{60}Fe must be invoked alongside WR winds to reproduce the ESS enrichment.
A supernova (SN) event is often cited as the ^{60}Fe source. However, recent models place an upper limit of 25M$_\odot$ on the initial mass of SN progenitors (Limongi & Chieffi 2018). This may preclude the same star from providing ^{26}Al through its WR winds *and* ^{60}Fe through supernova ejecta.

1.3 Direct Enrichment from Supernovae

Direct supernova enrichment is supported by numerous observations of protoplanetary discs within 1pc of a massive star (McCaughrean 1997; Smith et al. 2003; Oliveira et al. 2005; Marco et al. 2006).
Arguments for and against this mechanism as the origin of ^{26}Al and ^{60}Fe in the ESS come in several forms. Ouellette et al. (2007, 2010); Parker et al. (2014) and Lichtenberg et al. (2016) studied the process of injecting CCSN ejecta into a protoplanetary disc and found that the likelihood of achieving solar-level enrichment is low (<1%). Additionally, Scally & Clarke (2001); Adams et al. (2004) and Nicholson et al. (2019) determined that a protoplanetary disc in such close proximity to a massive star is likely to be destroyed before the supernova occurs. For discs that survive irradiation, Parker et al. (2023) and Patel et al. (2023) found that incorporating the progenitor's Wolf-Rayet (WR) winds enables greater levels of enrichment, making it easier to reproduce the ESS this way. The drawback here is that stellar feedback during this phase is likely to remove significant quantities of gas from the protoplanetary disc through photoevaporation, thereby precluding the formation of gas giants like Jupiter and Saturn.
However, it is worth noting that a star's natal gas may shield it from photoevaporation for a short time (~0.5Myr) which may help to avert disc destruction (Wilhelm et al. 2023).

1.4 Enrichment from AGB Stars

AGB stars are old, evolved stars undergoing violent ejections of their stellar material. The most massive AGBs (4-8M$_\odot$) can lose several M$_\odot$ of material during this phase (Höfner & Olofsson 2018). It has been shown that direct enrichment from AGB stars can reproduce the solar abundances of ^{26}Al and ^{60}Fe (Wasserburg et al. 2006; Trigo-Rodriguez et al. 2009; Parker & Schoettler 2023).
Since stars form in coeval clusters, it appears counter-intuitive to suggest that old, evolved stars should be found near newly formed ones. Through observations of AGBs near molecular clouds in the solar neighbourhood, Kastner & Myers (1994) found only a ~1% chance of an AGB interaction with a young star. Although the molecular cloud has up to a ~70% chance during its lifetime.
Despite this low prediction, the recent discovery of an AGB star interloping a star-forming region has offered further support to this mechanism as the source of SLR enrichment in the ESS (Parker & Schoettler 2023).

1.5 Triggered Sequential Star Formation

This mechanism decouples the enrichment of ^{26}Al and ^{60}Fe across multiple generations of stars. The former is provided by the winds of a massive star during its Main Sequence (MS) and WR phases, while the latter is delivered by supernovae.
This theory has strong foundations in the long-studied concept of triggered star formation from ionisation fronts and SN shockwaves (Elmegreen & Lada 1977; Preibisch & Zinnecker 1999; Elmegreen 2007; Hennebelle et al. 2009). Furthermore, hydrodynamical simulations have confirmed that SN shockwaves can trigger the collapse of protostellar cores (Boss & Keiser 2010; Li et al. 2014; Kinoshita et al. 2021). Meanwhile, the triggering of star formation in HII shells has been supported by observations in Deharveng & Zavagno (2010); Thompson et al. (2012); Duronea et al. (2017) and Palmeirim et al. (2017).
The complete model (see Figure 1), as detailed in Gounelle & Meynet (2012), is as follows:

(i) A first generation of stars forms at a time t = 0.

(ii) The first SNe begin to occur within a few Myr, ejecting ^{60}Fe into the host GMC.

(iii) At t ~ 5Myr, the surrounding regions of the GMC are enriched with a steady-state abundance of ^{60}Fe (balanced by radioactive decay and production from SNe).

(iv) At t ~ 10Myr, the SN shockwaves of the first generation trigger the formation of a second generation at a distance of ~20pc. Radioactive decay makes the genesis time of Generation #2 crucial to the final concentration of ^{60}Fe in the third generation.

(v) In this second generation, the winds of at least one massive star build up a region of dense ionised gas around 5-10pc in size, referred to as an HII shell. This arises through the balance between the photoionising radiation from the star which pushes out ionised gas, and the star's gravity which prevents its escape.

(vi) This shell is enriched with ^{26}Al via the winds of the massive star(s) during its lifetime. This is termed the 'collect' phase.

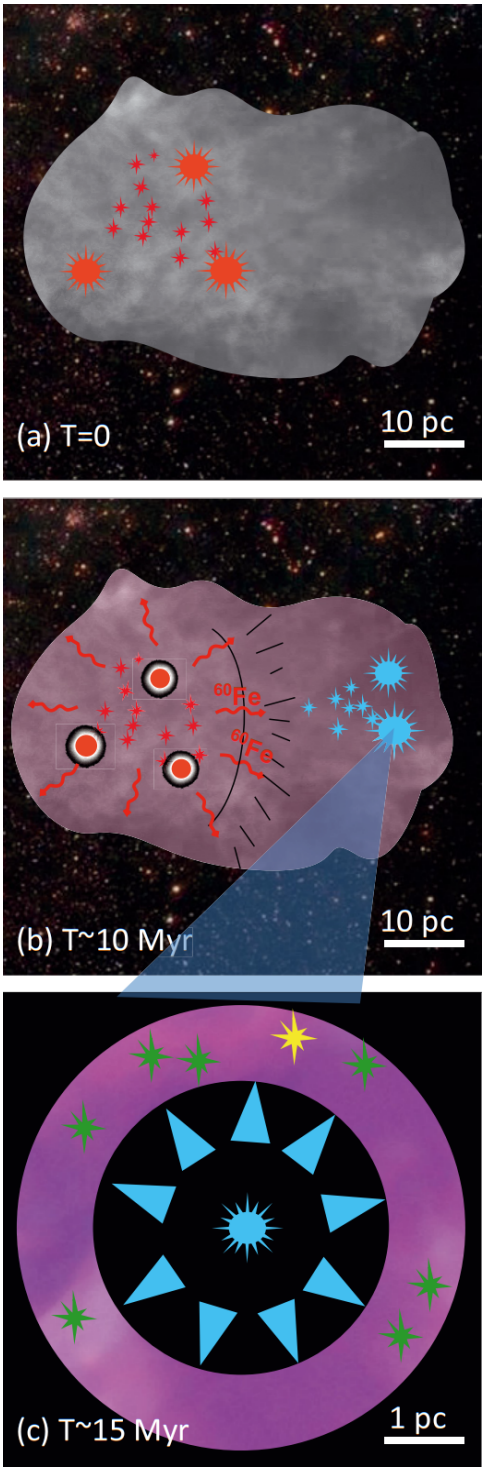

Figure 1. *Top Panel:* The first generation of stars (red) forms at t = 0.
Middle Panel: At t ~ 10Myr a steady-state enrichment of ^{60}Fe arises in the second region. The supernova shockwaves trigger a second generation of stars (blue) now enriched with ^{60}Fe.
Bottom Panel: At t ~ 15Myr an HII shell builds up which is then enriched with ^{26}Al by at least one massive star. The shell collapses into fragments, forming the third generation of stars (green/yellow) which are enriched with both ^{26}Al and ^{60}Fe.
Reproduced from Gounelle & Meynet (2012).

(vii) A third generation of stars then forms within this shell, enriched with both ^{26}Al and ^{60}Fe (this is the 'collect-and-collapse' mechanism).

To permit the formation of the third generation, the second must satisfy two constraints referred to throughout this paper as the 'double condition':

(i) Generation #2 must contain no more than 5 massive stars (>8M$_\odot$) to avoid the formation of 'superbubbles' – regions of hot, low-density gas several hundreds of pc across (Higdon & Lingenfelter 2005). Such superbubbles would prevent the formation of the HII shell which hosts Generation #3.

(ii) Generation #2 must contain at least one star with mass ≥32M$_\odot$ – the minimum mass required to enrich the third generation with enough ^{26}Al to match the ESS abundance.

This second condition comes from models of ^{26}Al yields from MS and WR winds. If the star is greater than 32M$_\odot$ then the SLR can be mixed into the HII shell with a wide range of efficiencies. Below 32M$_\odot$ however, and the efficiency must be greater than 1 (which by definition is impossible).
Gounelle & Meynet (2012) demonstrated that this mechanism is capable of reproducing the solar concentration ^{26}Al and ^{60}Fe with flexible parameters that could be tuned to account for a wide range of abundances of these isotopes. Despite this, no statistical analysis of this model is available, meaning its viability compared to other mechanisms remains unknown – an issue this study aims to remedy through Monte Carlo analysis.
In recent years the concept of triggered star formation has been challenged. Hydrodynamical simulations suggest that the observational indicators previously assumed to be evidence of triggered star formation may not be so (Dale et al. 2015). Additionally, the rapid expansion of newly formed clusters (Klessen & Kroupa 2001; Moeckel & Bate 2010; Parker & Meyer 2012; Parker & Dale 2013), would produce observable age spreads (or dichotomies) in sequentially triggered generations separated by less than ~40pc (Parker & Dale 2016). This characteristic may have been observed by Beccari et al. (2017) in the form of three populations in one cluster, each separated in age by 1Myr, although its findings were inconclusive. Thus, it is unclear whether presents an additional contradiction to the ideas presented by Gounelle & Meynet (2012).
Finally, the triggering of star formation in HII regions has also been challenged by Dale & Bonnell (2011) who argued that ionised gas fills low-density regions of the cloud, rather than these regions being excavated by massive stars. Despite this, there remains an undeniable association between HII shells and star formation. Since the model of enrichment via SSF simply requires star formation to occur in the vicinity of an HII shell (triggered or otherwise) its viability is unaffected by these findings.
In summary, the model presented in Gounelle & Meynet (2012) remains a plausible theory, able to produce enriched systems with a wide variety of SLR abundances – including ones that match the ESS.
This study will use theories of HII shells to verify the assumption that a solar-mass star can form in such an environment. Additionally, a statistical analysis via Monte Carlo simulation will be presented to determine two key results:

(i) The probability that three successive generations of stars will form via this mechanism.

(ii) The probability that a system enriched via this mechanism will contain an ^{60}Fe concentration matching that of the ESS.

Section 2 will present updates to the Gounelle & Meynet (2012) model based on recent findings pertaining to GMC lifetimes, before moving on to the methodology behind the simulation of ^{60}Fe ejection from supernovae and the Monte Carlo analysis. The results will be presented in Section 3, with the uncertainties and limitations of this study discussed in Section 4.

2 METHODOLOGY

2.1 Updating the 2012 Model

In the model presented by Gounelle & Meynet (2012), each generation of stars forms in the same Giant Molecular Cloud (GMC). However, the finite nature of GMC lifetimes necessitates adjustments to this description. Chevance et al. (2019) analysed a sample of GMCs and found that once massive stars become unembedded from their natal gas, their feedback effects drive the dispersion of the GMC within 1-5Myr. This period where massive stars coexist with the GMC was termed the 'feedback timescale'. Kim et al. (2021) used 24μm observations to trace embedded massive stars in GMCs which measured the full feedback timescale as 2-7Myr. Thus, once massive stars form, the GMC is destroyed within ~7Myr, meaning the first supernovae of Generation #1 are unlikely to occur within a molecular cloud. Indeed, 7Myr is the earliest possible supernova time in recent models (Schaller et al. 1992; Williams & Gaidos 2007; Limongi & Chieffi 2018).

Since the shockwave is not travelling through a GMC, the shock speed is likely to be on the order of a few thousand pc/Myr (Hughes et al. 2000; Ghavamian et al. 2002). Typical GMC separations of 438 – 912pc can be derived from the number densities given in Maeda et al. (2020) (see Section 2.5). Such distances would be traversed by the shockwave well within 1Myr, meaning this delay ($t_{\rm shock}$) is negligible when calculating the onset of Generation #2.

It is unknown how many shockwaves are required to trigger the collapse of a neighbouring GMC, with the answer likely depending on the progenitor masses, the density of the GMC, and its distance from the supernovae. Consequently, the median supernova time ($t_{\rm SN}$) is used as a proxy for the point at which collapse is triggered in the second GMC.

By sampling a cluster of 5 million stars from the IMF described in Kroupa (2001), the median SN time was calculated as 12.5Myr (see Section 2.3 for how SN detonation times are calculated in this study). Finally, the formation of Generation #2 is assumed to occur after one free-fall time of the GMC ($t_{\rm ff}$), which is taken to be 10Myr following Chevance et al. (2019).

Thus, with these simplifications, the onset of Generation #2 is assumed to be $t_2 = t_{\rm SN} + t_{\rm shock} + t_{\rm ff} \approx t_{\rm SN} + t_{\rm ff} = 22.5$Myr in all cases. The updated model of enrichment via SSF becomes:

(i) The first generation forms at t = 0.

(ii) At t = 2 – 7Myr, the GMC disperses leaving the cluster exposed.

(iii) After ~7Myr, the first SNe of Generation #1 begin to explode.

(iv) By t = 12.5Myr, the SN shockwaves trigger the collapse of the second GMC.

(v) After one free-fall time, the second generation forms at t = 22.5Myr.

(vi) At t > 22.5Myr, the third generation forms as described in Gounelle & Meynet (2012)

2.2 HII Region Analysis

To study the formation of solar mass stars in HII regions, it is first necessary to determine typical mass limits for these shells. The radius of the region of gas swept up into an HII shell is given by the following relation from Whitworth & Zinnecker (2004):

$$R_{\rm HII} = \left(\frac{3\dot{N}_{\rm Lye}}{4\pi\alpha n_0^2}\right)^{\frac{1}{3}} \quad (1)$$

Where $\dot{N}_{\rm Lye}$ is the rate of emission of ionising photons from the star at the centre of the shell, $\alpha \approx 2\text{x}10^{-13}$ cm^{3}s^{-1} and n_0 is the number density of Hydrogen nuclei in the region. By assuming a spherical region of gas is swept up and taking the mass density to be $m_{\rm p}n_0$, where $m_{\rm p}$ is the mass of a proton, the mass of the HII Region can be estimated as:

$$M_{\rm HII} = \left(\frac{m_{\rm p}\dot{N}_{\rm Lye}}{\alpha n_0}\right) = 4.2\text{x}10^{-45}\frac{\dot{N}_{\rm Lye}}{n_0} \quad (2)$$

Franco et al. (2000) gives typical number densities of HII Regions on the order of 100cm^{-3} while Schaerer & de Koter (1997) provides typical ionising fluxes on the order of 10^{48} – 10^{50} photons per second depending on the mass of the ionising star and the stage of its evolution. These values give mass limits of the HII Region at 42 to 4200M$_\odot$ which differ from the typical mass stated in Franco et al. (2000) of ~10^5M$_\odot$. As a result, the analysis in Section 3 will be based on the lower, more conservative estimate.

2.3 Initial Mass Functions and Ejecta Yields

Two models for the Initial Mass Function (IMF) of stellar clusters are used in this study. These are the Kroupa IMF (Kroupa 2001) and the Maschberger IMF (Maschberger 2013). The parameters used for the Kroupa IMF were:
$m_0 = 0.08$M$_\odot$
$m_1 = 0.1$M$_\odot$
$m_2 = 0.5$M$_\odot$
$m_3 = 150$M$_\odot$
$\alpha_1 = 0.3$
$\alpha_2 = 1.3$
$\alpha_3 = 2.3$.

The Maschberger IMF was programmed with parameters of:
$m_l = 0.1$M$_\odot$
$m_u = 120$M$_\odot$
$\alpha = 2.3$
$\beta = 1.4$
$\mu = 0.2$.

Cumulative distributions of stellar masses are plotted for both models in Figure 2. Both of these models are used in the analysis to obtain an indication of how this uncertainty affects the final results. In addition, three different supernova models are used to determine the yield of ^{60}Fe from the initial cluster (Woosley & Weaver 1995; Limongi & Chieffi 2006, 2018). The data used from each source was for non-rotating, solar-metallicity stars with all three models taking the WR contribution into account when calculating the total yield.

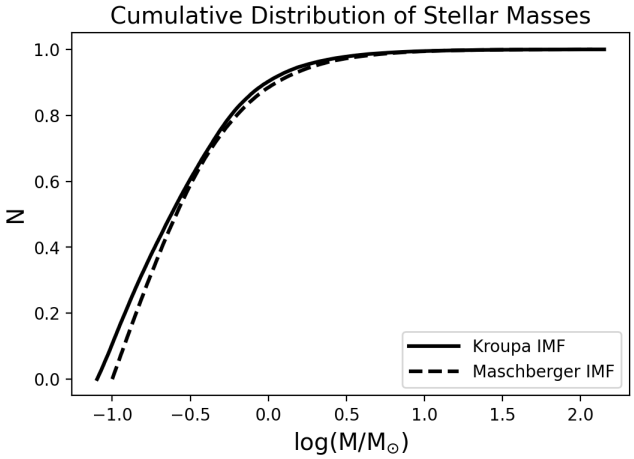

Figure 2. The two IMF models produce similar mass distributions in stellar clusters. The Maschberger IMF has a slightly lower proportion of low-mass stars.

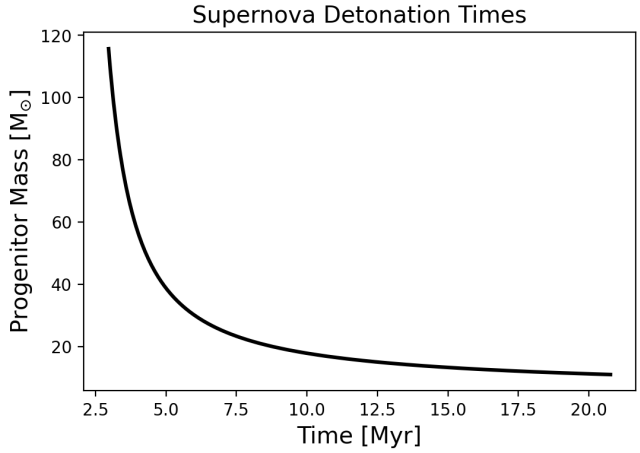

Figure 4. The supernova detonation times from the relation of $\log(t_{SN}) = 1.4/\log(M)^{1.5}$ (Schaller et al. 1992; Williams & Gaidos 2007). The highest progenitor masses have the earliest detonations. As progenitor mass decreases, detonation times get further apart.

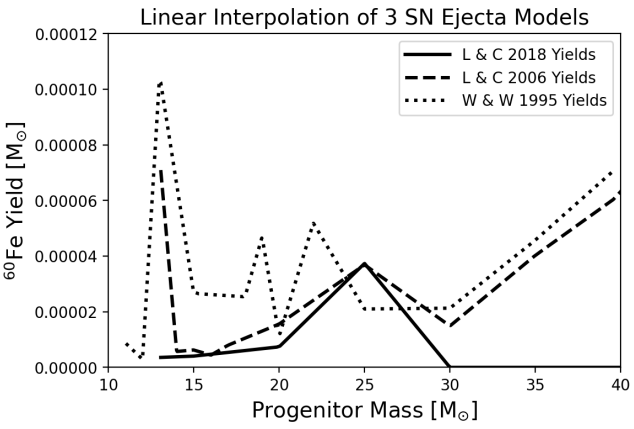

Figure 3. Woosley & Weaver (1995) give the highest yields of ^{60}Fe for low-mass (<25M$_\odot$) progenitors, but stop at the 40M$_\odot$ limit. The two Limongi & Chieffi models are very different since the 2018 models drop to zero after the 25M$_\odot$ point, while the 2006 yields continue rising to the 120M$_\odot$ limit (meaning they produce the highest ^{60}Fe yields of the three).

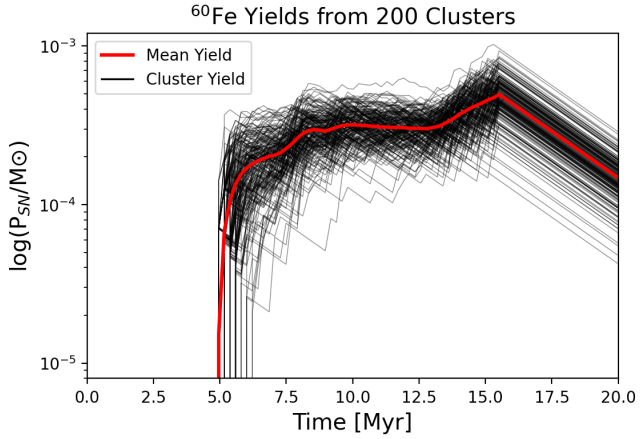

Figure 5. Using the Woosley & Weaver (1995) yields, 200 clusters, each containing 10,000 stars, were generated with the Maschberger IMF. P_{SN} was calculated for each cluster from t = 0 to t = 20Myr (shown by the black lines). The red line traces the mean value of $\log(P_{SN})$ for the 200 clusters.

The primary difference between these models is the mass limits of the progenitor stars. Woosley & Weaver (1995) provides data for progenitors in the 11 – 40M$_\odot$ range, whereas for Limongi & Chieffi (2006), this mass range is 11 – 120M$_\odot$. Limongi & Chieffi (2018) uses a mass range of 13 – 120M$_\odot$ but the initial-mass limit for a supernova progenitor is 25M$_\odot$ meaning all stars above this mass contribute ^{60}Fe from their winds alone – i.e. with no supernova contribution. See Figure 3 for comparisons of the 3 yield models used in this study.

The supernova times used in this study follow the equation given in Williams & Gaidos (2007) of $\log(t_{SN}) = 1.4/\log(M)^{1.5}$ based on an empirical fit to the data in Schaller et al. (1992). Progenitor mass is plotted against supernova time in Figure 4. The two IMFs are combined with the three ejecta models to create 6 cases used in the simulation – these are summarised in Table 2.

2.4 Modelling ^{60}Fe Enrichment

At a time t, the amount of *non-decayed* ^{60}Fe obtained from a cluster, P_{SN}, is defined as:

$$P_{SN} = \sum_{i=1}^{N_{SN}} Y_{SN_i} e^{-\frac{(t-t_i)}{\tau_{60}}} \quad (3)$$

where N_{SN} is the total number of supernovae in the cluster, Y_{SN_i} is the yield from ith supernova occurring at time t_i, and τ_{60}=3.7Myr is the mean lifetime of ^{60}Fe. Figure 5 displays the results from calculating P_{SN} for 200 clusters of 10,000 stars.

A cluster with a greater number of stars is likely to yield more ^{60}Fe. The relationship between cluster population and yield can be studied by generating many clusters with varying sizes and taking the mean yield at a given time for each cluster size. For 1,000 clusters at 6 different population sizes, ranging from 10 to 100,000 stars, a linear relationship was found where $\overline{P}_{SN} = k_{SN} N_1$ (see Figure 6).

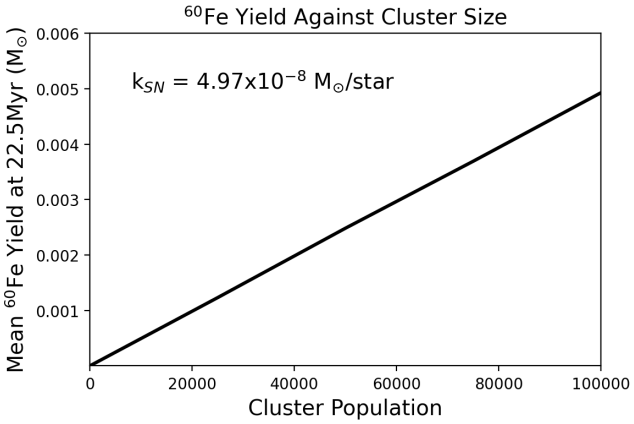

Figure 6. The mean yield at t = 22.5Myr for 1,000 clusters at 6 different population sizes is shown for Case F – the Maschberger IMF with the Woosley & Weaver (1995) yields. Cluster population and ^{60}Fe yield share a linear relationship. This relationship holds for all six combinations of IMF and ejecta model which in each case is quantified by the parameter $k_{\rm SN}$.

Case	IMF	Ejecta Yields	$k_{\rm SN}$ (M$_\odot$ per star)
A	Kroupa	Limongi & Chieffi (2018)	8.04x10^{-9}
B	Kroupa	Limongi & Chieffi (2006)	1.60x10^{-7}
C	Kroupa	Woosley & Weaver (1995)	3.87x10^{-8}
D	Maschberger	Limongi & Chieffi (2018)	1.01x10^{-8}
E	Maschberger	Limongi & Chieffi (2006)	2.07x10^{-7}
F	Maschberger	Woosley & Weaver (1995)	4.97x10^{-8}

Table 2. These 6 cases represent every combination of the different models used in this study. For each case, the mean quantity of non-decayed ^{60}Fe per star present at the onset of Generation #2, $k_{\rm SN}$, is shown in the right-hand column.

This proportionality allows for the definition of the parameter $k_{\rm SN}$ as the average amount of non-decayed ^{60}Fe per star in Generation #1 present at the onset of Generation #2 (ignoring any dilution effects). The value of $k_{\rm SN}$ for each of the 6 cases described in Section 2.3 are shown in Table 2.

This relationship between cluster population and ^{60}Fe yield enables the derivation of an equation describing the concentration of this SLR in the final generation of stars, first laid out in Gounelle & Meynet (2012).

It has been shown that $\overline{P}_{\rm SN} = k_{\rm SN} N_1$. Accounting for the geometrical dilution of the ejecta as it travels to the second GMC, the concentration of ^{60}Fe in this location, C, is defined as:

$$C = \gamma \frac{\overline{P}_{\rm SN}}{M_2} = \gamma \frac{k_{\rm SN} N_1}{M_2} \tag{4}$$

where M_2 is the mass of the second GMC and γ is the geometrical dilution factor (see Section 2.5 for how this is defined). M_2 can be related to the population of the second cluster, N_2 by $\epsilon M_2 = \widetilde{m}_\star N_2$ where ϵ is the star formation efficiency (SFE) and $\widetilde{m}_\star$ is the mean stellar mass in Generation #2.

As a result, the concentration equation becomes:

$$C = \frac{\gamma \epsilon k_{\rm SN} N_1}{\widetilde{m}_\star N_2} \tag{5}$$

Finally, incorporating the radioactive decay of ^{60}Fe between the onset of the second and third generations results in the final form of this equation:

$$C = \frac{\gamma \epsilon k_{\rm SN} N_1}{\widetilde{m}_\star N_2} e^{-t/\tau_{60}}, \tag{6}$$

where t is the time between the onset of Generation #2 and that of Generation #3.

The final concentration of ^{60}Fe is calculated for each iteration of the Monte Carlo simulation, following the methodology described in the following sections.

2.5 Modelling Ejecta Dilution

A simple model of an expanding shell of material was used to represent the geometrical dilution of the SN ejecta. Firstly, the geometrical dilution factor, γ, was defined as the dimensionless ratio between the final and initial ejecta densities, i.e. $\gamma = \rho_{\rm f}/\rho_{\rm i}$ where γ<1 for an expanding shell.

For a shell of ejecta material with mass M, the density of the shell is given by:

$$\rho = \frac{3M}{4\pi\left(r_{\rm out}^3 - r_{\rm in}^3\right)} \tag{7}$$

where $r_{\rm in}$ and $r_{\rm out}$ are the inner and outer radii of the shell respectively. Assuming a small shell thickness, dr, it follows that $r_{\rm out}^3 = (r_{\rm in} + dr)^3$. Expanding the brackets and taking dr to be small enough for terms in dr^2 to be neglected, it can be shown that $r_{\rm out}^3 = r_{\rm in}^3 + 3r_{\rm in}^2 dr$. Substituting this into Equation 7 gives:

$$\rho = \frac{M}{4\pi r_{\rm in}^2 dr} \tag{8}$$

Exploiting the simplifying assumption that the shell's thickness, dr, remains constant throughout the expansion, means that the ratio of the final and initial densities can be written as:

$$\gamma = \frac{\rho_{\rm f}}{\rho_{\rm i}} = \frac{M}{4\pi R_{\rm f}^2 dr} \frac{4\pi R_{\rm i}^2 dr}{M} = \left(\frac{R_{\rm i}}{R_{\rm f}}\right)^2 \tag{9}$$

where $R_{\rm i}$ and $R_{\rm f}$ are the inner edges of the shell before and after expansion respectively.

Thus, Equation 6 becomes:

$$C = \left(\frac{R_{\rm i}}{R_{\rm f}}\right)^2 \frac{\epsilon k_{\rm SN} N_1}{\widetilde{m}_\star N_2} e^{-t/\tau_{60}} \tag{10}$$

The outstanding task is to assign definitions to $R_{\rm i}$ and $R_{\rm f}$. The latter is taken as the distance the ejecta travels before encountering the second GMC. Defining the former is less clear-cut and, as a result, two extreme cases are used in this study.

Firstly, in the most generous case, the cluster as a whole is assumed to eject one collective shell in a scenario referred to in this paper as 'cluster-scale' dilution. Here, $R_{\rm i}$ is equal to the radius of the first cluster. In the strictest case – referred to as 'stellar-scale' dilution, the initial radius is reduced to a little larger than the size of the SN progenitor. Here, $R_{\rm i}$ is taken to be several $R_\odot \approx 10^{-7}$pc.

Under the assumptions that $R_{\rm i}$ and $R_{\rm f}$ are the same for all shells, and that all SNe eject the same mass of material, the definition remains $\gamma = (R_{\rm i}/R_{\rm f})^2$ in all cases.

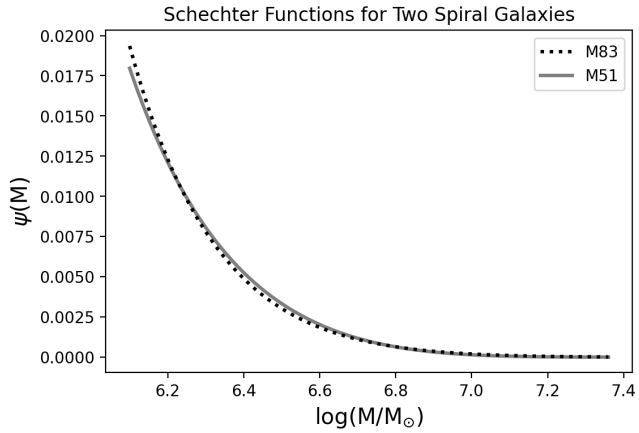

Figure 7. The two Schechter functions for M51 and M83 are shown. The probability of selection, $\psi(\mathrm{M})$, is plotted against GMC mass. The similarity between the two made the choice between them arbitrary. The values of $\psi(\mathrm{M})$ were normalised to sum to 1.

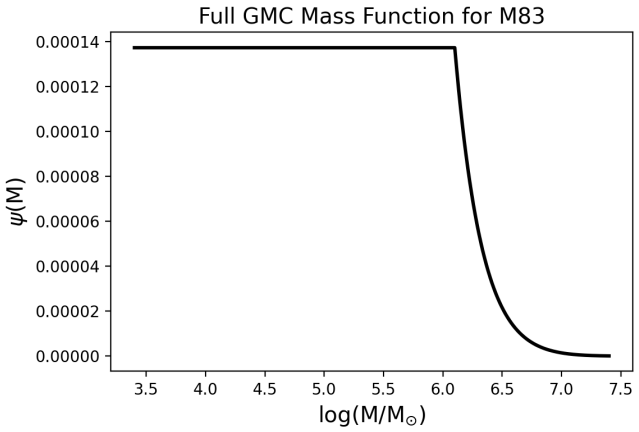

Figure 8. The full GMC mass function used in this simulation is shown. It is the combination of the flat distribution from $10^{3.4}$ – $10^{6.1}$ and the M83 Schechter function from Mok et al. (2020). The probability of selection, $\psi(\mathrm{M})$, is plotted against GMC mass. The values of $\psi(\mathrm{M})$ were normalised to sum to 1.

In the Monte Carlo simulation, both dilution models were analysed. For the case of cluster-scale dilution, R_i was selected from a flat distribution between limits of 0.1 – 25pc (Pfalzner 2009). In the case of stellar-scale dilution, R_i was set to 10^{-7}pc.
The definition of R_f uses observational data of GMC number densities from Maeda et al. (2020). Observations of NGC 1300 yielded results for the number of GMCs per kpc^2 in the range of 1.2 to 5.2. The typical separation implied by the number density, n, is calculated as $1/\sqrt{n}$. Thus, limits of 438 – 912pc were derived for the distance between GMCs #1 and #2. R_f is selected from a flat distribution between these limits, regardless of the definition of R_i.

2.6 Calculating Cluster Populations

The cluster populations, N_1 and N_2, are not chosen from their own distribution. Rather, for each population, a GMC mass, M_GMC, is chosen alongside a star formation efficiency, ϵ, and the population is simply calculated as $N = \epsilon M_\mathrm{GMC}/\widetilde{m}_\star$.
The SFEs are chosen from a flat distribution between the limits of 0.002 – 0.2 (Murray 2011). The SFE for Generation #2 is the one used in Equation 6 to calculate the final ^{60}Fe concentration.
The GMC masses are chosen from a Schechter function (a mathematical description of the drop-off at the high end of the GMC mass function). There are no Schechter function parameters available for the Milky Way. A power law relation is available (Rosolowsky 2005), yet this is a less accurate description of the shape of the GMC mass function.
Mok et al. (2020) presents Schechter function parameters for a sample of galaxies, two of which (M51 and M83) are included here due to their classification as spiral galaxies. The drop-off at the high end of the mass function is shown for both galaxies in Figure 7. The similarity of the two Schechter functions made the choice between them arbitrary, and it was M83 that was chosen for the simulation. Mok et al. (2020) states that the mass function flattens for masses below the drop-off point ($\sim 10^{6.1}\mathrm{M}_\odot$ for M83). Thus, it was assumed that the rest of the distribution is perfectly flat down to the lower mass limit of $\sim 10^{3.4}\mathrm{M}_\odot$ provided by Lada & Dame (2020). The entire GMC mass function used in the simulation is displayed in Figure 8.
This method of calculating cluster populations provided reasonable limits of ~10 to 8 million stars (with the largest populations being far less likely to occur). At the start of the drop-off, the largest possible population is ~420,000 stars.
Such a broad range of GMC masses highlights the computational limitations of this study. The mass must be drawn from a set of linearly spaced values – each weighted according to the mass function. Yet, if a small number of increments is used across a 4dex range, the proportion of values in the lower orders of magnitude will be accentuated. In a linear space across this range, a larger set of values will more accurately portray the range it occupies. It can be seen from Figure 9 that selection from a smaller set of values will produce an inflated proportion within the lower orders of magnitude.
This is important to the final results as only populations under 2,000 stars may pass the double condition. This means that if clusters of this size are being selected more than is statistically reasonable, the proportion of successful runs will be overestimated.
Due to computational limitations, the analysis of a pass/fail of the double condition (see next section) was carried out independently of the ^{60}Fe concentration analysis. The former used a set of 20,000 values across the GMC mass range whereas the latter (which was more computationally demanding) used only 200.

2.7 Testing the Second Cluster

As described in Section 1.5, the second cluster must pass the double condition to be capable of producing a third generation of stars enriched with ^{26}Al and ^{60}Fe. The probability that a cluster will pass this double condition is plotted as a function of cluster size for both IMFs in Figure 10.
The likelihood of producing enriched systems via SSF strongly depends on the proportion of Generation #2 clusters that pass the double condition. To test this, a population is calculated as in the previous section and a prediction is made to determine pass or fail.
It can be seen from Figure 10 that clusters larger than 2,000 stars do not pass the double condition. In addition, the minimum value used in this analysis was 10 stars. Thus, if the size of the cluster is outside these limits, it is immediately counted as a fail. If the cluster population falls within these limits, the following procedure is used to obtain a pass or fail:

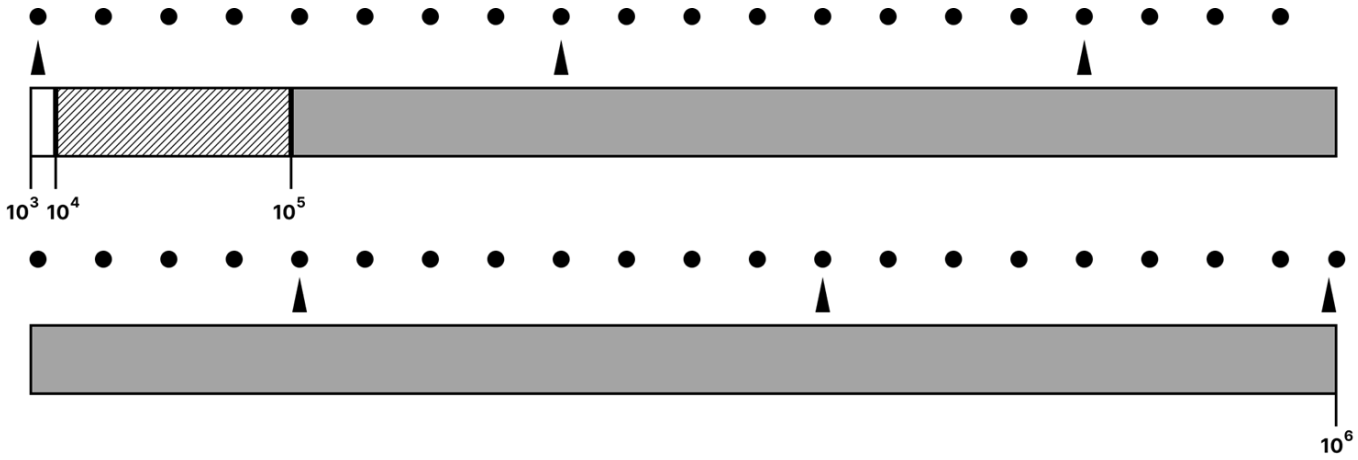

Figure 9. The unfilled region represents the 10^3 order of magnitude, the lined region 10^4, and the filled region 10^5. The circles and triangles display the positions of two linearly spaced sets of values across a 3dex range. When selecting values from the triangle set, 16.7% will lie within the 10^3 range. When selecting from the circle set, a more accurate proportion of 2.4% lies in this range.

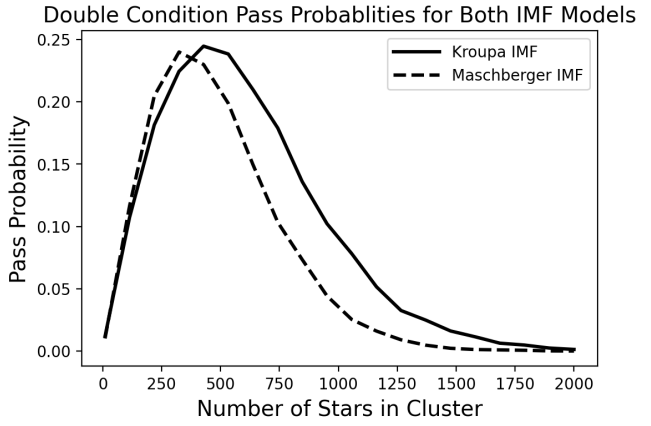

Figure 10. The probability of a cluster containing no more than 5 massive stars (>8$M_\odot$) and at least one star >32$M_\odot$ plotted as a function of cluster population. The probability of clusters passing this double condition shows significant variation between the two IMFs.

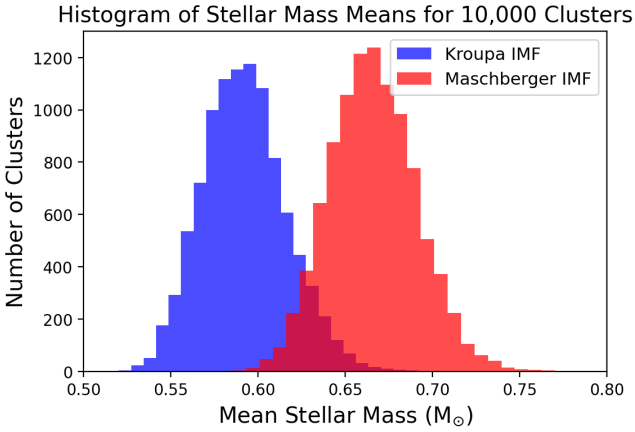

Figure 11. The mean stellar mass of a sample of 10,000 stars was calculated 10,000 times for the Kroupa IMF (blue) and the Maschberger IMF (red). Histograms of the results display the Gaussian nature of the distributions.

(i) The cluster's size has been calculated as N stars.

(ii) The shape of the pass-probability curve for the appropriate IMF is interpolated.

(iii) The probability of this cluster of N stars passing the double condition is determined.

(iv) A random number between 0 and 1 is chosen.

(v) If this number is less than the pass probability, it is considered a pass and the final ^{60}Fe concentration is calculated. Otherwise, it is considered a fail and the final concentration is set to zero.

In this way, a statistically accurate proportion of clusters between 10 and 2,000 stars passes the double condition. Throughout this paper, runs of the Monte Carlo simulation resulting in a pass are referred to as 'successful' – note this does not mean solar-level enrichment was achieved, just that *some* level of enrichment was achieved.
Overall, the proportion of second-generation clusters that pass the double condition determines the likelihood that *any* enrichment will occur via this mechanism.

2.8 Determining Mean Stellar Mass

The mean stellar mass for each IMF can be calculated by taking the mean mass of a sample of stars. However, upon each calculation, the mean varies. If this is repeated many times, a Gaussian distribution builds up (as shown in Figure 11). The mean, μ, and standard deviation, σ, of these distributions were calculated for each IMF. For the Kroupa IMF, $\mu = 0.59$ and $\sigma = 0.02$, while for the Maschberger IMF, $\mu = 0.665$ and $\sigma = 0.02$.
For each iteration of the simulation, a mean stellar mass is chosen from the appropriate distribution (as determined by the IMF used in each case, see Table 2).

2.9 Additional Decay Time

The parameter t in Equation 6 depends on the amount of time it takes for the 'collect-and-collapse' mechanism to produce a third generation of stars. In other words, the time taken after Generation #2 is formed for the HII shell to form and collapse to form Generation #3.

The analysis in Gounelle & Meynet (2012) used ^{26}Al yields from the winds of massive stars to determine that there are many scenarios which reproduce the solar concentration of this SLR. The range of acceptable times between the two generations was calculated as 1.15 – 6.70Myr.

For the Monte Carlo simulation in this study, a value of t is chosen from a flat distribution between these limits. There is an important assumption here in that, no matter the time taken to form Generation #3, it always receives a concentration of ^{26}Al matching that of the ESS.

One of the main limitations of this study is that only ^{60}Fe enrichment is analysed. The potential impact on the final results of including ^{26}Al enrichment is discussed in Section 4.3.

2.10 Defining Solar Concentration

The measured abundance of ^{60}Fe in the ESS is somewhat controversial, with measurements covering a 2dex range with a ^{60}Fe/^{56}Fe mass ratio, $Z_{\mathrm{Fe}} \sim 10^{-8} - 10^{-6}$. This ratio can be converted into a concentration of ^{60}Fe in parts per billion. Following the calculations in Parker & Schoettler (2023) and using measurements of isotopic abundances of the ESS from Lodders (2003), the mass of ^{56}Fe is given by:

$$M_{^{56}\mathrm{Fe}} = 1828\mathrm{x}10^{-4} M_{\mathrm{dust}} \tag{11}$$

where M_{dust} is the mass of dust in the protoplanetary disc. Assuming $M_{\mathrm{dust}} = 0.001\mathrm{M}_{\odot}$, the ^{56}Fe is $1.828\mathrm{x}10^{-4}\mathrm{M}_{\odot}$. Thus, the mass of ^{60}Fe can be calculated using $M_{^{60}\mathrm{Fe}} = Z_{\mathrm{Fe}} M_{^{56}\mathrm{Fe}}$. The resulting range of measurements for the solar concentration of ^{60}Fe is 0.0018 – 0.18ppb.

These values are therefore taken as a broad set of limits for the concentration of ^{60}Fe in the ESS. Any simulated system for which the ^{60}Fe concentration falls within this range is considered to be a reproduction of the ESS. The proportion of simulations that fit into this category indicates the probability that this mechanism will produce a system like the Solar System.

A summary of all parameters used in the Monte Carlo simulation, their limits, selection method, and source, is presented in Table 3.

3 RESULTS

3.1 Solar-Mass Star Formation in HII Regions

A key assumption in this model is that a solar mass star could form from the material gathered into an HII shell. Mass limits for the HII region of 42 – 4200$M_{\odot}$ were derived in Section 2.2.

To verify this assumption, clusters were generated star-by-star until a cluster mass limit was reached. At this point, the cluster was analysed to check if a solar-mass star was present. This was repeated for many clusters at various mass limits. The proportion of clusters (at each given mass) with at least one star between 0.9 and 1.1$M_{\odot}$ was taken as the probability of forming a solar-mass star from that amount of star-forming material.

The results of this analysis are shown in Figure 12. Beyond a cluster mass of ~20M$_{\odot}$, it is more likely than not that a solar-mass star will form. This cluster mass, however, is *not* the mass of star-forming material available – i.e. the mass of the HII shell. An estimate of the mass of pre-stellar material can be obtained from the star formation efficiencies for HII regions of 2 – 5% (Wilson & Matthews 1995). This implies a pre-stellar mass of 400 – 1,000M$_{\odot}$ for a cluster mass of 20M$_{\odot}$. Thus, only the very lowest estimates of HII shell mass make the formation of a solar-mass star unlikely. As a result, it is an acceptable assumption to make that a solar-mass star can form in an HII shell.

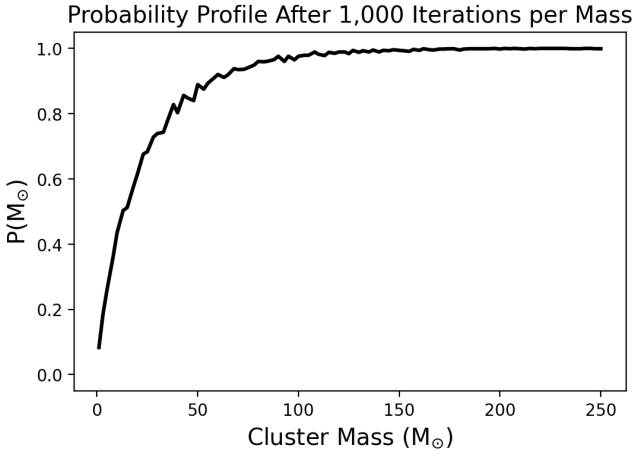

Figure 12. P($M_{\odot}$) is the proportion of clusters containing at least one star with a mass between 0.9 and 1.1$M_{\odot}$. This proportion tends to 1 as cluster mass increases.

3.2 The Probability of a Successful Run

As mentioned in Section 2.7, the proportion of second-generation clusters that pass the double condition dictates the likelihood of forming a third generation of stars. By extension, this indicates the probability that a first-generation cluster can go on to provide the ^{60}Fe enrichment (and trigger the subsequent ^{26}Al enrichment) of a solar-mass star.

With the constraints of the double condition fixed, the only factor impacting the chance of a pass is the choice of IMF. Hence, it is only necessary to simulate 2 of the 6 cases in Table 2. Cases A (Kroupa IMF) and D (Maschberger IMF) were chosen here. After 1 million runs each, the proportion of successful runs was 0.11% for the Kroupa IMF and 0.093% for the Maschberger IMF. In other words, ~1 in 1000 clusters that form may go on to generate a system enriched with ^{26}Al and ^{60}Fe.

3.3 The Probability of Solar Enrichment

If only ~0.1% of runs generate an enriched system, this produces a sample of only 1,000 for the analysis of ^{60}Fe concentrations. To generate a larger sample, the population of the second generation was not calculated as described in Section 2.6. Instead, the double condition pass probability for each IMF (shown in Figure 10) was used to assign weightings to populations from 10 to 2,000 that would be selected at random. Consequently, the populations drawn reflect those that would pass the double condition if the original procedure was followed.

Using this method, 1 million successful runs were carried out for all 6 Cases and the final concentrations of ^{60}Fe were analysed. The

Parameter	Description	Value/Range	Selection Method	Source
k_{SN}	Mean yield of ^{60}Fe per star in Cluster #1	See Table 2	Pre-defined (Cases A – F)	See Section 2.4
τ_{60}	Mean Lifetime of ^{60}Fe	3.7Myr	Pre-defined	Rugel et al. (2009)
R_i (stellar-scale dilution)	Initial Radius of Ejecta Shell (several $R_\odot$)	10^{-7}pc	Pre-defined	See Section 2.5
R_i (cluster-scale dilution)	Radius of Cluster #1	0.1 – 25pc	Random selection (flat distribution)	Pfalzner (2009)
R_f	Distance between GMCs #1 & #2	438 – 912pc	Random selection (flat distribution)	Maeda et al. (2020)
t	Time between onset of Generations #2 & #3	1.15 – 6.70Myr	Random selection (flat distribution)	Gounelle & Meynet (2012)
ϵ_1, ϵ_2	Star Formation Efficiency in GMCs #1 & #2	0.002 – 0.2	Random selection (flat distribution)	Murray (2011)
$M_{GMC,1}$, $M_{GMC,2}$	Masses of GMCs #1 & #2	$10^{3.40}$ – $10^{7.36}$	Random selection (mass function)	Lada & Dame (2020); Mok et al. (2020)
$\widetilde{m}_\star$	Mean Stellar Mass	Kroupa: (μ=0.59, σ=0.02) Maschberger: (μ=0.665, σ=0.02)	Random selection (Gaussian distribution)	See Section 2.8
N_1	Population of Cluster #1	~10 – 10^6	Calculation	$\epsilon_1 M_{GMC,1}/\widetilde{m}_\star$
N_2	Population of Cluster #2	~10 – 10^6	Calculation	$\epsilon_2 M_{GMC,2}/\widetilde{m}_\star$
γ	Geometrical Dilution Factor	Stellar-Scale: (1.2 – 5.2)x10^{-20} Cluster-Scale: 1.2x10^{-8} – 3.3x10^{-3}	Calculation	$(R_i/R_f)^2$

Table 3. All parameters and calculations used in the Monte Carlo simulation are listed above alongside their permitted range and the method used to select a value for each parameter. Where references are not given, the appropriate calculation or Methodology subsection is cited.

results of this simulation are summarised in Table 4.
The probabilities of 27.5% – 59.5% for solar enrichment displayed in Table 4 are not outright probabilities for the reproduction of the ESS. To obtain these, the probability of a successful run must be taken into account. For the scenario of cluster-scale dilution, this produces outright probabilities in the range of 0.026% – 0.065%. Stellar-scale dilution is unable to reproduce the concentration of ^{60}Fe in the ESS due to the extremely low concentrations that result from it.
Probability distributions for cases A, B, and C (Kroupa IMF with each of the 3 ejecta models) with cluster-scale dilution are plotted in Figure 13. The skewed shape of the histograms, with the longer tail towards the low concentrations, is due to the drop-off in the GMC mass function at the high end. This makes the slope at high concentrations steeper since the highest cluster sizes (and therefore highest yields of ^{60}Fe) are less likely to occur.

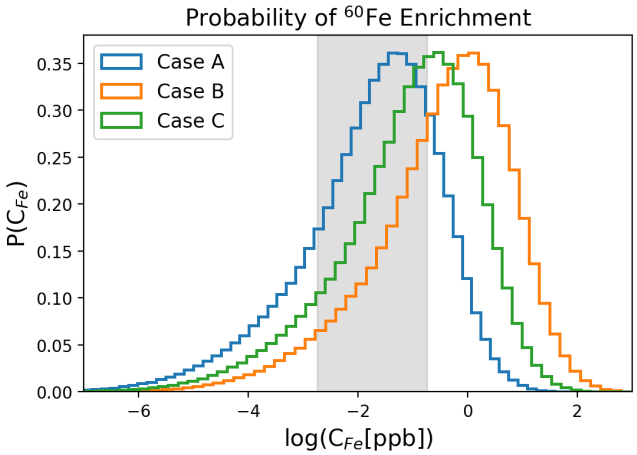

Figure 13. Probability distributions for the various ^{60}Fe concentrations produced by 1 million successful runs are shown for cases A – C under cluster-scale dilution. The grey region represents the limits for solar enrichment as defined in Section 2.10.

4 DISCUSSION

The method used to estimate the masses of HII shells was highly simplified. The greatest simplification was the assumption that the density of the sphere of radius R_{HII} was the same as the density of the HII shell. In reality, the gas surrounding the star gets compressed into the shell, meaning the HII-shell density taken from Franco et al. (2000), and subsequently used in Equation 2, is larger than the theorised sphere.
This is why the mass estimate obtained in Section 2.2 is significantly lower than the mass given by Franco et al. (2000). Even with this low estimate, it was shown that a solar-mass star is very likely to form from such quantities of pre-stellar material. Therefore, this aspect of

Case	% Solar Enrichment R_i = 0.1 – 25pc	Median Enrichment (ppb) R_i = 0.1 – 25pc	% Solar Enrichment $R_i = 10^{-7}$pc	Median Enrichment (ppb) $R_i = 10^{-7}$pc
A	59.5	0.025	0.0	$2.45\text{x}10^{-18}$
B	29.8	0.50	0.0	$4.89\text{x}10^{-17}$
C	44.8	0.12	0.0	$1.19\text{x}10^{-17}$
D	58.2	0.031	0.0	$3.03\text{x}10^{-18}$
E	27.5	0.64	0.0	$6.22\text{x}10^{-17}$
F	42.3	0.15	0.0	$1.50\text{x}10^{-17}$

Table 4. This table displays results from the ^{60}Fe concentration analysis for successful runs only. For each case, 1 million successful runs were simulated under each dilution model. The percentage of runs producing a system with an ^{60}Fe concentration between 0.0018 and 0.18ppb (the range defined as a match to the ESS) is shown in the second and fourth columns.

the model does not affect the statistical likelihood of achieving SLR enrichment via this mechanism.

For cluster-scale dilution of SN ejecta, ~27-60% of successful runs reproduce the ^{60}Fe enrichment of the ESS. However, due to the narrow constraints on the second generation, this proportion falls to ~0.05% for all runs.

When stellar-scale dilution is used, the dilution factor is on the order of 10^{-20}. Such extreme values reduced the median enrichment of the final generation by a factor of $\sim 10^{-16}$, making it effectively impossible to reproduce the ^{60}Fe concentration of the ESS.

The 0.065% yielded by the 'best-case scenario' is significantly lower than the ~1% found by recent studies of direct SN enrichment (Parker et al. 2023; Patel et al. 2023) and the ~1% interaction rate of young stars with AGBs predicted by Kastner & Myers (1994).

Any increase in the amount of dilution would shift all the distributions shown in Figure 13 to lower concentrations, thereby reducing the proportion of ESS reproductions. Furthermore, even if every successful run produced solar-level enrichment, the probability is still limited to ~0.1% (the proportion of successful runs). As a result, enrichment via sequentially formed clusters appears less viable than direct enrichment, either by CCSNe or AGB stars.

Many uncertainties exist within the parameters of this Monte Carlo simulation. This section will split their discussion into those most impactful to the proportion of successful runs, and those most impactful to the probability of ESS reproduction. Finally, the limitations of this study and prospects for future work will be discussed.

4.1 Uncertainties Within the Probability of a Successful Run

The proportion of runs that successfully produce a third generation of stars is solely dependent on the likelihood of the second cluster passing the double condition, which acts as a statistical bottleneck in the process. As explained in Section 1.5, these constraints are that the second cluster must contain no more than 5 stars with mass >8M$_\odot$, and at least one star with mass ≥32M$_\odot$.

The chance of a pass is dependent on three things: the IMF used, the nature of the two constraints, and the size of the second cluster. The effect of changing the IMF was minimal – a shift from 0.11% for the Kroupa IMF to 0.093% for the Maschberger IMF. The effect of relaxing either of the two constraints was more pronounced. The following analysis uses data from the Kroupa IMF alone.

Reducing the minimum mass required for the enriching star from 32M$_\odot$ to 16M$_\odot$ gave a total pass probability of 0.23%. This would increase the 'best case' chance of reproducing the ESS ^{60}Fe enrichment from 0.065% to 0.14%. The pass probability here is shown as a function of cluster size in Figure 14.

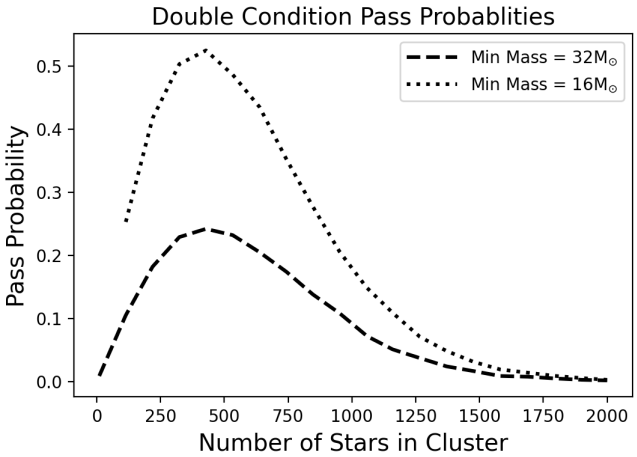

Figure 14. The original distribution for double-condition pass probability is shown alongside the distribution for the looser constraint on the mass of the ^{26}Al-enriching star. Both datasets were produced using the Kroupa IMF.

This constraint is determined by the stellar evolution models used to calculate ^{26}Al enrichment of the HII shell. Greater yields of ^{26}Al would allow for a lower-mass enriching star, thereby increasing the chance of solar-level enrichment. Conversely, lower yields would reduce the probability.

Reverting to the 32M$_\odot$ minimum and increasing the limit on the number of massive stars in the cluster from 5 to 10 resulted in a broader range of cluster sizes that could pass the double condition. This had the strongest impact on pass probability, with 1.2% of second-generation clusters satisfying both conditions.

Such an increase would result in ~0.7% of runs producing solar-level enrichment. Once again, the pass probability as a function of cluster size is compared to the original in Figure 15.

This constraint is defined by the physics of superbubble formation in molecular clouds, a phenomenon which would preclude the formation of an HII shell. Advancements in this field could potentially have a significant effect on the viability of this model as a mechanism of ^{60}Fe enrichment.

Presently, there is no reason to believe these constraints should be loosened, but this analysis serves to demonstrate the significant de-

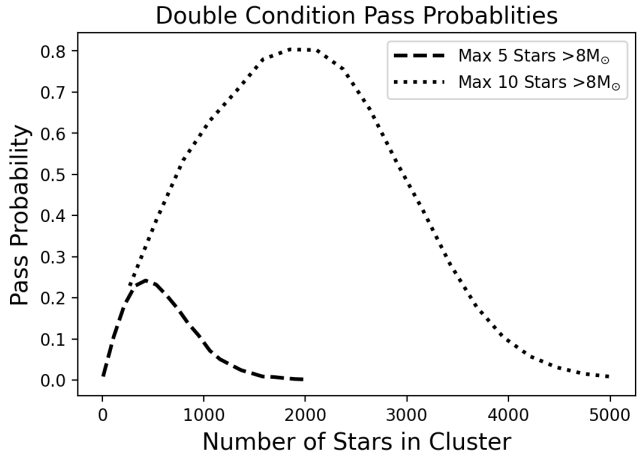

Figure 15. The effect on double-condition pass probability of increasing the number of massive stars permitted in the second cluster is shown. The range of cluster sizes that may pass the double condition has broadened from 10-2000 under the 5-star limit, to 10-5000 under the 10-star limit. Both datasets were produced with the Kroupa IMF.

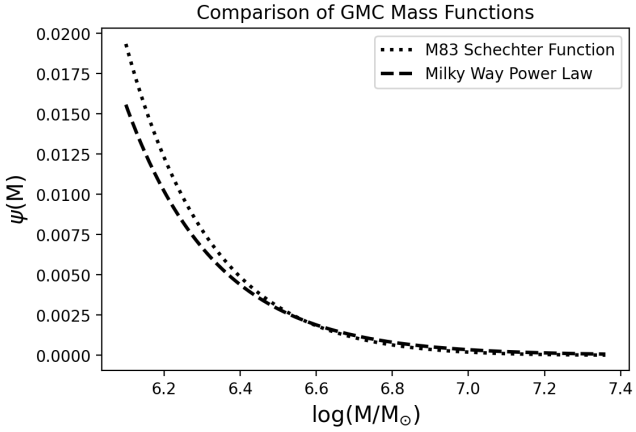

Figure 16. The power law for the GMC mass function of the Milky Way is compared to the Schechter function the the M83 spiral galaxy. The probability of selection, $\psi(\mathrm{M})$, is plotted against GMC mass. The values of $\psi(\mathrm{M})$ were normalised to sum to 1.

pendence of this model on the properties of the second cluster.

The final aspect determining the proportion of successful runs is the size of the second cluster. Consequently, the method used to calculate cluster population becomes important. For example, if the limits of cluster size are broadened, the proportion of selected populations within the window of 10 to 2,000 stars will be reduced – thus lowering the probability of a successful run.

In principle, the method of using a GMC mass function, in conjunction with an appropriate SFE and mean stellar mass, will produce a statistically accurate sample of cluster populations. However, the implementation of this method was subject to numerous simplifications and inaccuracies.

Firstly, the Schechter function used does not apply to the Milky Way (because no Schechter parameters are available for a Milky Way GMC mass function). Despite this, the high-end drop-off modelled by the Milky Way power law (Rosolowsky 2005) follows a very similar shape to the M83 Schechter function (see Figure 16), making the choice between them fairly ineffectual.

Secondly, the mass function below the start of the drop-off was assumed to be perfectly flat down to the lower mass limit. Thus, there is no 'hump' in the middle of the distribution, nor is there a sloped drop-off at the low end. While the mass function constructed was acceptable for this study, the absence of these features reduces the accuracy of this method.

The third reason this method could not be implemented with complete efficacy is the method of selecting the SFE for each GMC. The assumption of a flat distribution between 0.002 and 0.2 may be subject to the following inaccuracies:

(i) The probability distribution may not be flat.
(ii) The density and velocity profiles of the GMC impact SFE (making the SFE location-dependent within the GMC).
(iii) SFE is correlated with free-fall time (Murray 2011).
(iv) SFE is dependent on the age of the GMC (Murray 2011).

The first inaccuracy listed above could have a significant effect on the results of this study as it could skew the sample of second-generation populations towards (or away from) the 10 – 2,000-star window required for a pass. Thus altering the proportion of successful runs.

The correlation with GMC age and free-fall time introduces a systematic error in selecting a random SFE since these factors are unaccounted for in the probability distribution and range of appropriate SFEs.

The final part of the simulation impacting the chance of a successful run is the lack of a relation between Generations #1 and #2. The populations are calculated independently of each other – each is simply calculated from a randomly chosen GMC mass, SFE, and mean stellar mass. This generates realistic cluster populations, yet does not account for the triggered formation of the second by the first.

Since the two clusters are linked in this way, it may be unreasonable to suggest that an initial cluster of 10 stars could trigger the formation of a million-star cluster (or vice versa). Yet, this is possible in the simulation presented in this study.

The size of the first cluster may constrain the size of the second – perhaps to a Gaussian distribution centred around the population of Generation #1. Using this method, the population of the second generation would always be close to that of the first. However, since the selection of the first population would still follow the original method, the sample of second-generation populations would be largely unaffected by this change. Consequently, changing the model in this way shouldn't have a significant impact on the proportion of successful runs.

A more impactful alternative to the independent selection of the two cluster sizes would be to assume that the size of the second cluster must be some proportion of the first. Modelling this as a 'triggering efficiency' with a flat distribution between 0.001 and 0.5 increased the probability of a successful run from 0.11% to 0.97%. This is because the upper limit for the population of Generation #2 is reduced and smaller clusters become more likely to occur. This increases the proportion within the window of 10 – 2,000 stars.

It should also be noted that the set of 20,000 values applied across the GMC mass range was deemed sufficient for this part of the analysis. This is because the final result tended to ~0.1% as the size of the value-set was increased. It can be seen from the data in Table 5 that larger value sets would produce results below 0.1%, but the difference would be minor.

Collectively, these uncertainties could have a significant impact on the probability of a successful run – conceivably raising it to a few per cent. This would improve the viability of enrichment via SSF,

Size of Value-Set	Chance of Successful Run
20	6.9%
200	0.87%
2,000	0.18%
20,000	0.11%

Table 5. The larger sets of values for selection from the GMC mass range produce a smaller proportion of successful runs. This is because the proportion of selections that fall within the lower orders of magnitude is inflated with small value sets, making the larger sets more accurate.

although its favourability over direct enrichment would not be definitive.

4.2 Uncertainties Within the Probability of Solar Enrichment

Despite the low likelihood of a successful run, the proportion that produces solar-level enrichment can be as high as ~60%. However, this percentage is heavily influenced by the choices of dilution and ejecta models, and the accuracy of the k_{SN} parameter.

Firstly, the ejecta yields had a reasonable impact – shifting the likelihood of solar enrichment by ~30%. However since the lowest proportion is still significant (~27%), it remains possible to reproduce solar-level enrichment regardless of the chosen ejecta model.

The dominant factor in the final concentration is the dilution model. It has been shown that the two extremes can change the median enrichment by a factor of $\sim 10^{16}$. Such vast shifts take the case of solar-level enrichment from a rare event to an impossibility.

Uncertainties within the dilution model arise in numerous places. Firstly, the approximations used to derive Equation 9 (namely the constant, small shell thickness) will not hold in reality. It is more likely that the shell boundaries disperse as it expands, increasing the thickness and further diluting the ejecta.

An additional assumption of this dilution model is that the ejecta travels, unobstructed, to the second GMC. It is then assumed that the ejecta is fully incorporated into the pre-stellar material upon arrival. In reality, it is possible that some ejecta is buffered before reaching the region, or that some ejecta passes through the region without being incorporated. In this sense, this model provides an upper limit to the final concentration in Generation #3.

A final consideration is the 'clumpiness' of supernova ejecta (Pan et al. 2012) which would undermine the assumption that the ejecta shell is of uniform concentration at all times. This would introduce a degree of unpredictability – higher concentrations would be more likely, yet enrichment, in general, would be more rare.

There is an intrinsic uncertainty in using k_{SN} to determine the yield of ^{60}Fe from a cluster. The value of k_{SN} is calculated from the mean mass of ^{60}Fe ejected from 10,000 clusters. However, as can be seen in Figure 5, there is a significant spread around the mean.

Deviations from the mean are greater for smaller cluster sizes. This is because a cluster of 10 stars, for example, may contain no SN progenitors when simulated, yet the calculation from k_{SN} will always yield some amount of ^{60}Fe.

Figure 17 shows how the disparity between the yield calculated using k_{SN} and the yield from a simulated cluster of the same number of stars varies with cluster size. For the smallest clusters, the simulated yield was on average a factor of 2 away from the calculated yield. The difference began to plateau at around 37% for large clusters (>10,000 stars). Thus, in the Monte Carlo simulation, the calculated yield in each run comes with at least a ~30% uncertainty, which rises to ~200% for the smallest clusters.

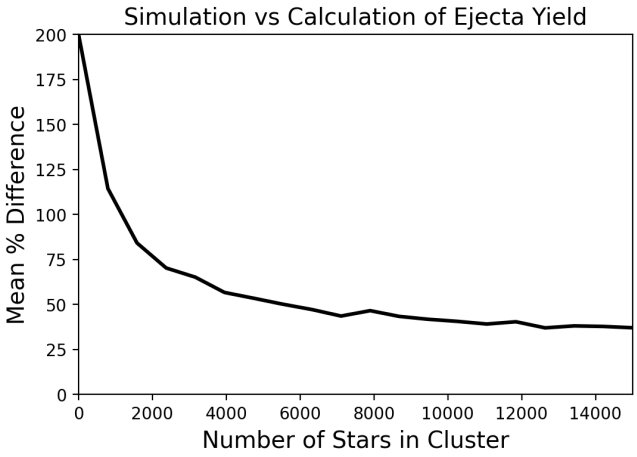

Figure 17. Using the models for Case A only, the mean percentage difference between calculation and simulation of the ejecta yield is plotted against cluster population. The mean was calculated over 100 clusters at each size. The smallest clusters contain the largest errors between the two yields.

The primary effect of this uncertainty is to inflate the likelihood of the lowest concentrations since even the smallest clusters are guaranteed to contribute some ^{60}Fe.

It should also be noted that the small set of 200 linearly spaced values applied across the 4dex range for GMC mass (see Section 2.6) will have inflated the likelihood of a lower level of enrichment. This is because smaller clusters of stars are disproportionately likely to be selected by the Monte Carlo simulation. This will have also contributed to the skewed shape of the histograms in Figure 13. Computational limitations prevented the use of a larger set of values.

A further uncertainty is that k_{SN} is dependent on the point in time when the second generation forms. This could feasibly be anywhere between the arrival of the first and last shockwaves but was taken to be the median SN time. Additionally, it was assumed that the second cluster is formed after one GMC free-fall time, but this is merely an indication of how long GMC collapse may take and does not represent how quickly Generation #2 will form. Finally, it was also assumed that all GMCs have a free-fall time of 10Myr. While this is acceptable as a typical value, it is not true that this extends to all GMCs in the Milky Way.

These assumptions lead to a significant uncertainty in how much Fe60 has decayed before the onset of Generation #2, which affects the calculation of k_{SN} and, in turn, creates a systematic error in the calculated ^{60}Fe yields from all clusters.

4.3 Limitations and Scope for Future Work

One of the main limitations of this study was computing power. Some parameter models relied on averages to define their values (e.g. k_{SN}, mean stellar mass). In addition, due to the nature of Monte Carlo simulations, the results themselves will differ slightly each time the simulation is run. This effect is reduced through a large number of iterations (1 million in this study), yet computing power places limits on how many iterations can be run.

Limitations in computing power also reduced the accuracy of selecting values from the GMC mass function, as was discussed in Sections 2.6 and 4.2.

There are aspects of this mechanism that remain unstudied by this project. The most notable is an analysis of the ^{26}Al yields from massive stars. These are crucial to this model as they not only determine the concentration of ^{26}Al in the final generation, but they also determine one of the constraints in the double condition – the most important bottleneck in the process. The results reported here only consider ^{60}Fe enrichment, although combining this with ^{26}Al enrichment would provide a more complete analysis.

This would also serve to better define the additional decay time used in Equation 6. The range used in this study is simply the range that could conceivably produce solar-level enrichment of ^{26}Al. The assumption made in Section 2.9 that all runs receive the solar concentration of ^{26}Al introduces a significant bias.

A more impartial way to model this process would be to build a model for the collect-and-collapse phase which provides typical times for the onset of Generation #3. Then, using models of ^{26}Al ejection, a yield can be calculated at the time of collapse which gives the concentration in the final generation. Since solar concentrations would have to be matched by this SLR *and* by ^{60}Fe, the proportion of runs matching the ESS would likely be significantly reduced.

The fact that the two clusters remain independent of each other in this simulation is an issue. As such, further research is required into how one cluster may be generated by the supernovae of another. This would provide important insight into this part of the mechanism, thereby allowing a much more reliable study of its viability.

Furthermore, due to the substantial uncertainties in the dilution model and the ^{60}Fe yield calculations, the best test of this mechanism's viability would be a simulation of the entire process. A study such as this would require a hydrodynamical simulation of the triggered formation of a cluster from GMC over-densities induced by SN shockwaves. From this, the exact yield, decay, and dilution of the ejecta can be determined – thereby removing the most significant uncertainties in this analysis. Furthermore, by simulating the collect-and-collapse phase in an HII shell, the ^{26}Al concentration can be accurately determined.

Until simulations of this complexity are computationally possible, the viability of this mechanism is difficult to determine with great precision. However, the analysis presented here indicates that it is less likely to be the source of ^{26}Al and ^{60}Fe in the ESS than direct enrichment from SNe or AGB stars.

5 CONCLUSION

It has been shown through Monte Carlo simulation that the enrichment of planetary systems with ^{26}Al and ^{60}Fe via sequential star formation is less likely to occur than the direct enrichment from CC-SNe or AGB stars. This is primarily due to the statistical bottleneck presented by the narrow constraints placed on the second generation of stars.

The uncertainties within this methodology do not allow for enough of a deviation from the reported results to make this mechanism significantly more viable than direct enrichment. Indeed, the most substantial uncertainty, the dilution model, may entirely rule out this mechanism as a possible source of SLRs in the ESS, as it appears that only the most generous models provide a sufficient ^{60}Fe concentration.

Future work should combine ^{26}Al yields with the findings presented here. Additionally, full hydrodynamical simulations will be crucial in discerning the exact nature of this process, and its viability as the source of SLR enrichment in the ESS.

REFERENCES

Adams F. C., 2010, Annual Review of Astronomy and Astrophysics, 48, 47
Adams F. C., Hollenbach D., Laughlin G., Gorti U., 2004, The Astrophysical Journal, 611, 360
Alves F. O., Cleeves L. I., Girart J. M., Zhu Z., Franco G. A., Zurlo A., Caselli P., 2020, The Astrophysical Journal Letters, 904, L6
Arnould M., Paulus G., Meynet G., 1997, Astronomy and Astrophysics, v. 321, p. 452-464, 321, 452
Arnould M., Goriely S., Meynet G., 2006, Astronomy & Astrophysics, 453, 653
Beccari G., et al., 2017, Astronomy & Astrophysics, 604, A22
Boss A. P., Keiser S. A., 2010, The Astrophysical Journal Letters, 717, L1
Busso M., 2018, The Early Solar System. Springer International Publishing, Cham, pp 379–425, doi:10.1007/978-3-319-91929-4_6, https://doi.org/10.1007/978-3-319-91929-4_6
Chevance M., et al., 2019, Monthly Notices of the Royal Astronomical Society, 493, 2872
Crowther P. A., 2007, Annu. Rev. Astron. Astrophys., 45, 177
Dale J. E., Bonnell I., 2011, Monthly Notices of the Royal Astronomical Society, 414, 321
Dale J., Haworth T., Bressert E., 2015, Monthly Notices of the Royal Astronomical Society, 450, 1199
Deharveng L., Zavagno A., 2010, Proceedings of the International Astronomical Union, 6, 239–246
Diehl R., et al., 2006, Nature, 439, 45
Duprat J., Tatischeff V., 2007, The Astrophysical Journal, 671, L69
Duronea N. U., Cappa C. E., Bronfman L., Borissova J., Gromadzki M., Kuhn M., 2017, Astronomy & Astrophysics, 606, A8
Elmegreen B. G., 2007, The Astrophysical Journal, 668, 1064
Elmegreen B. G., Lada C. J., 1977, Astrophysical Journal, Part 1, vol. 214, June 15, 1977, p. 725-741., 214, 725
Franco J., Kurtz S., García-Segura G., Hofner P., 2000, Astrophysics and Space Science, 272, 169
Ghavamian P., Winkler P. F., Raymond J. C., Long K. S., 2002, The Astrophysical Journal, 572, 888
Gilmour J., Middleton C., 2009, Icarus, 201, 821
Gounelle M., Meynet G., 2012, Astronomy & Astrophysics, 545, A4
Gounelle M., Shu F. H., Shang H., Glassgold A. E., Rehm K. E., Lee T., 2006, The Astrophysical Journal, 640, 1163
Hennebelle P., Mac Low M., Vazquez-Semadeni E., 2009, Structure Formation in Astrophysics, p. 205
Higdon J., Lingenfelter R., 2005, The Astrophysical Journal, 628, 738
Höfner S., Olofsson H., 2018, The Astronomy and Astrophysics Review, 26, 1
Hughes J. P., Rakowski C. E., Decourchelle A., 2000, The Astrophysical Journal, 543, L61
Jacobsen B., et al., 2011, The Astrophysical Journal Letters, 731, L28
Kastner J. H., Myers P. C., 1994, ApJ, 421, 605
Kim J., et al., 2021, Monthly Notices of the Royal Astronomical Society, 504, 487
Kinoshita S. W., Nakamura F., Wu B., 2021, The Astrophysical Journal, 921, 150
Klessen R., Kroupa P., 2001, Astronomy & Astrophysics, 372, 105
Kroupa P., 2001, Monthly Notices of the Royal Astronomical Society, 322, 231
Lada C. J., Dame T., 2020, The Astrophysical Journal, 898, 3
Li S., Frank A., Blackman E. G., 2014, Monthly Notices of the Royal Astronomical Society, 444, 2884
Lichtenberg T., Parker R. J., Meyer M. R., 2016, Monthly Notices of the Royal Astronomical Society, 462, 3979
Lichtenberg T., Golabek G. J., Burn R., Meyer M. R., Alibert Y., Gerya T. V., Mordasini C., 2019, Nature Astronomy, 3, 307
Limongi M., Chieffi A., 2006, The Astrophysical Journal, 647, 483
Limongi M., Chieffi A., 2018, The Astrophysical Journal Supplement Series, 237, 13
Lodders K., 2003, The Astrophysical Journal, 591, 1220
Lugaro M., Doherty C. L., Karakas A. I., Maddison S. T., Liffman K., Garcia-

Hernandez D. A., Siess L., Lattanzio J. C., 2012, Meteoritics & Planetary Science, 47, 1998
Lugaro M., Ott U., Kereszturi , 2018, Progress in Particle and Nuclear Physics, 102, 1
Maeda F., Ohta K., Fujimoto Y., Habe A., 2020, Monthly Notices of the Royal Astronomical Society, 493, 5045
Marco O. D., O'Dell C. R., Gelfond P., Rubin R. H., Glover S. C. O., 2006, The Astronomical Journal, 131, 2580
Maschberger T., 2013, Monthly Notices of the Royal Astronomical Society, 429, 1725
McCaughrean M. J., 1997, in International Astronomical Union Colloquium. pp 546–548
McDonough W. F., Šrámek O., Wipperfurth S. A., 2020, Geochemistry, Geophysics, Geosystems, 21, e2019GC008865
Moeckel N., Bate M. R., 2010, Monthly Notices of the Royal Astronomical Society, 404, 721
Mok A., Chandar R., Fall S. M., 2020, The Astrophysical Journal, 893, 135
Murray N., 2011, The Astrophysical Journal, 729, 133
Nicholson R. B., Parker R. J., Church R. P., Davies M. B., Fearon N. M., Walton S. R. J., 2019, Monthly Notices of the Royal Astronomical Society, 485, 4893
Oliveira J. M., Jeffries R. D., van Loon J. T., Littlefair S. P., Naylor T., 2005, Monthly Notices of the Royal Astronomical Society: Letters, 358, L21
Ouellette N., Desch S. J., Hester J. J., 2007, The Astrophysical Journal, 662, 1268
Ouellette N., Desch S. J., Hester J. J., 2010, The Astrophysical Journal, 711, 597
Palmeirim P., et al., 2017, Astronomy & Astrophysics, 605, A35
Pan L., Desch S. J., Scannapieco E., Timmes F., 2012, The Astrophysical Journal, 756, 102
Parker R. J., Dale J. E., 2013, Monthly Notices of the Royal Astronomical Society, 432, 986
Parker R. J., Dale J. E., 2016, Monthly Notices of the Royal Astronomical Society, 456, 1066
Parker R. J., Meyer M. R., 2012, Monthly Notices of the Royal Astronomical Society, 427, 637
Parker R. J., Schoettler C., 2023, The Astrophysical Journal Letters, 952, L16
Parker R. J., Church R. P., Davies M. B., Meyer M. R., 2014, Monthly Notices of the Royal Astronomical Society, 437, 946
Parker R. J., Lichtenberg T., Patel M., Polius C. K. M., Ridsdill-Smith M., 2023, Monthly Notices of the Royal Astronomical Society, 521, 4838
Patel M., Polius C. K. M., Ridsdill-Smith M., Lichtenberg T., Parker R. J., 2023, Monthly Notices of the Royal Astronomical Society, 525, 2399
Pfalzner S., 2009, Astronomy & Astrophysics, 498, L37
Pfalzner S., et al., 2015, Physica Scripta, 90, 068001
Podosek F. A., Nichols Robert H. J., 1997, AIP Conference Proceedings, 402, 617
Preibisch T., Zinnecker H., 1999, The Astronomical Journal, 117, 2381
Rosolowsky E., 2005, Publications of the Astronomical Society of the Pacific, 117, 1403
Rugel G., et al., 2009, Phys. Rev. Lett., 103, 072502
Scally A., Clarke C., 2001, Monthly Notices of the Royal Astronomical Society, 325, 449
Schaerer D., de Koter A., 1997, Astronomy and Astrophysics, v. 322, p. 598-614, 322, 598
Schaller G., Schaerer D., Meynet G., Maeder A., 1992, Astron. and Astrophys. Suppl. Ser.—1992.—96.—P, pp 269–331
Smith N., Bally J., Morse J. A., 2003, The Astrophysical Journal, 587, L105
Thielemann F.-K., Isern J., Perego A., Von Ballmoos P., 2018, Space Science Reviews, 214, 62
Thompson M. A., Urquhart J. S., Moore T. J. T., Morgan L. K., 2012, Monthly Notices of the Royal Astronomical Society, 421, 408
Tissot F. L., Dauphas N., Grove T. L., 2017, Geochimica et Cosmochimica Acta, 213, 593
Trigo-Rodriguez J. M., Garcia-Hernandez D. A., Lugaro M., Karakas A. I., van Raai M., Lario P. G., Manchado A., 2009, Meteoritics & Planetary Science, 44, 627
Wang W., et al., 2007, Astronomy & Astrophysics, 469, 1005
Wasserburg G. J., 1985, in Black D. C., Matthews M. S., eds, Protostars and Planets II. pp 703–737
Wasserburg G., Busso M., Gallino R., Nollett K., 2006, Nuclear Physics A, 777, 5
Whitworth A. P., Zinnecker H., 2004, Astronomy & Astrophysics, 427, 299
Wilhelm M. J. C., Portegies Zwart S., Cournoyer-Cloutier C., Lewis S. C., Polak B., Tran A., Mac Low M.-M., 2023, Monthly Notices of the Royal Astronomical Society, 520, 5331
Williams J. P., Gaidos E., 2007, The Astrophysical Journal, 663, L33
Wilson C. D., Matthews B. C., 1995, arXiv preprint astro-ph/9506104
Woosley S., Weaver T. A., 1995, Technical report, The evolution and explosion of massive Stars II: Explosive hydrodynamics and nucleosynthesis. Lawrence Livermore National Lab.(LLNL), Livermore, CA (United States)

This paper has been typeset from a TEX/LATEX file prepared by the author.